# An integrated and multi-purpose microscope for the characterization of atomically thin optoelectronic devices

Adolfo De Sanctis, Gareth F. Jones, Nicola J. Townsend, Monica F. Craciun, and Saverio Russo[*]

*Centre for Graphene Science, College of Engineering, Mathematics and Physical Sciences, University of Exeter, Exeter EX4 4QF, United Kingdom*

E-mail: S.Russo@exeter.ac.uk

## Abstract

Optoelectronic devices based on graphene and other two-dimensional (2D) materials, such as transition metal dichalcogenides (TMDs) are the focus of wide research interest. They can be the key to improving bandwidths in telecommunications, capacity in data storage, new features in consumer electronics, safety devices and medical equipment. The characterization these emerging atomically thin materials and devices strongly relies on a set of measurements involving both optical and electronic instrumentation ranging from scanning photocurrent mapping to Raman and photoluminescence (PL) spectroscopy. Furthermore, proof-of-concept devices are usually fabricated from micro-meter size flakes, requiring microscopy techniques to characterize them. Current state-of-the-art commercial instruments offer the ability to characterize individual properties of these materials with no option for

---

[*]To whom correspondence should be addressed

arXiv:1609.07514v3 [physics.ins-det] 3 Oct 2016

the *in situ* characterization of a wide enough range of complementary optical and electrical properties. Presently, the requirement to switch atomically-thin materials from one system to another often radically affects the properties of these uniquely sensitive materials through atmospheric contamination. Here, we present an integrated, multi-purpose instrument dedicated to the optical and electrical characterization of devices based on 2D materials which is able to perform low frequency electrical measurements, scanning photocurrent mapping, Raman, absorption and PL spectroscopy in one single set-up with full control over the polarization and wavelength of light. We characterize this apparatus by performing multiple measurements on graphene, transition metal dichalcogenides (TMDs) and Si. The performance and resolution is equivalent to commercially available instruments with the significant added value of being a compact, multi-purpose unit. Our design offers a versatile solution to face the challenges imposed by the advent of atomically-thin materials in optoelectronic devices.

Since the discovery of graphene,[1,2] the ability to isolate atomically thin materials has attracted growing interest within the scientific community owing to a unique set of unprecedented properties suddenly available on a single chip.[3,4] Two-dimensional semiconductors are currently enabling conceptually new devices, including light detectors and emitters,[5] transistors[6] and memories.[7] The characterization of such devices strongly relies on a set of techniques which combine electrical, optical and spectroscopic measurements. For example, inelastic light scattering (Raman) spectroscopy has been the main tool to study the properties of graphene and its derivatives,[8] while photodetectors based on 2D materials have been largely characterized by Scanning Photocurrent Microscopy (SPCM). To characterize both light-emitting and detecting devices, the knowledge of optical parameters such as the absorption and reflection coefficients of the material is of paramount importance. Commercial instruments are usually used to perform these characterizations in distinct self-standing systems which requires transport of the sample in different environments and retrofitting to accommodate the different holders designed for each specific tool.

In this work, we present an experimental apparatus developed to characterize optoelectronic devices based on graphene and other 2D materials. Centred around an upright metallurgical microscope, this system allows us to perform multiple measurements in one instrument, with no need to remove the device from its holder, reducing the risk of contamination or breakage. These measurements include: low frequency electrical transport, SPCM, absorption (transmittance and reflectance), micro-Raman, photoluminescence (PL) and electroluminescence (EL) spectroscopy and mapping, with or without polarized light. A unique aspect of the developed design is the ability to concurrently perform both the electrical and optical measurements. The system is equipped with multiple laser sources, spanning from UV to red light and two white light sources used for transmission and reflection illumination. Our design delivers the laser light in enclosed paths and an interlock system cuts the laser light to allow access to individual parts, making it extremely safe. High spatial resolution in spectroscopy and SPCM measurements is achieved by diffraction-limited focusing of Gaussian laser beams and a high performance microscope stage. Electrical connections are secured by a custom-built PCB board, designed to reduce electrical noise and allow easy access to devices, without the need for long working distance microscope objectives.

We characterize the instrument with a series of standard measurements: SPCM on graphene-based photodetectors as well as absorption, Raman and PL spectroscopy of a range of 2D materials and organic semiconductors. We prove its high functionality and demonstrate that the achieved resolution, both spatial and spectroscopic, and the overall performance, is equivalent to current commercial technologies, with the additional benefit of having a compact, multi-purpose, fully customizable, instrument with the potential for installation of additional measurement features.

# I  Operating principles

Light-matter interaction is at the heart of optoelectronic devices.[9,10] These work by converting an electric signal into light or *vice-versa*. For this reason their design requires knowledge of both the optical and electrical characteristics of the materials used. In this section we will review the fundamental principles of light detection and emission, with focus on atomically-thin devices, and the associated measurement techniques, such as SPCM. We will also review the fundamentals of the spectroscopy techniques, absorption, Raman and PL, which allow the optical properties of the active materials to be studied. The two main categories in which optoelectronic devices are divided are light emitters (LED) and photodetectors (PDs).

## I.A  Light emission and detection in atomically thin devices

To characterize LEDs, it is necessary to be able to electrically drive the light emission mechanism whilst recording the spectrum and power of the emitted light. The electrical input can be DC, in the case of injection-devices such as p-n junction diodes,[10] or AC, as required by alternating current electroluminescent (ACEL) devices.[11] The spectral analysis of the emitted radiation is used to gain insight into the physics of the light-emitting material. This is usually achieved by efficiently collecting the emitted light and delivering it to a high-resolution spectrometer with minimal losses or aberrations in the optical path. High spatial resolution can be achieved by employing a microscope lens to collect the light. In this way the area of the LED can be accurately mapped, enabling the study of gradients, defects, inhomogeneities or the presence of localized

emitters.

To characterize a PD, the basic experiment consists of shining light onto the device and recording its electrical response, such as measuring the current flow through it or a change in resistance.[10] Light can impinge on the whole surface of the device, known as flood illumination, or it can be delivered with a focused laser onto a specific area to allow for a spatially resolved photo-response. Both techniques give insight on the physical nature of the observed photoresponse and on the efficiency of the device. In general, the magnitude of the generated photocurrent is given by:[10]

$$I_{ph} = q\eta_i \frac{P^\beta}{\hbar\nu}(1 - \exp^{-\alpha\delta}),\tag{1}$$

where $\eta_i = (I_{ph}/q)/\phi_{abs}$ is the internal quantum efficiency of the PD, defined as the number of charges, $q$, collected to produce the photocurrent $I_{ph}$, divided by the number of absorbed photons $\phi_{abs}$, $P_{opt}$ is the incident optical power, $\hbar\nu$ is the energy of the photons, $\alpha$ is the absorption coefficient of the material (see section I.B) and $\delta$ its thickness. The exponent $\beta$ depends on the photocurrent generation mechanism, in general it is equal to 1 for photovoltaic (PV) devices. A summary of the main quantities used to characterize LEDs and PDs is given in Table 1.

In graphene and TMDs several mechanisms are responsible for the observed photocurrent.[12] The most widely used technique to study such devices is SPCM, where a laser beam is scanned across the device and the electrical response recorded at each point, producing a two-dimensional map of the photoresponse.[13] SPCM allows the study of spatially resolved properties of optoelectronic devices, where the spatial resolution is ultimately defined by the laser spot size, $d_s$. Improvements in spatial resolution have been achieved by the use of near-field techniques, such as scattering scanning near-field optical nanoscopy (s-SNOM).[12] SPCM has been used, for example, to study the dynamics of hot carriers in graphene PDs,[14] to demonstrate the role of defects in observed photocurrent signals[14] and to characterize the photoactive regions in TMDs junctions.[15]

## I.B  Absorption spectroscopy

Design and characterization of optoelectronic devices requires the optical properties of the photoactive materials, coatings and electrodes to be known. As shown in Equation (1) the absorption

Table 1: Parameters typically used to characterize optoelectronic devices. Coupling Factors and the wavelength dependence of all quantities is omitted for clarity of notation.

| Quantity | Symbol | Definition[a] |
|---|---|---|
| External Quantum Efficiency | $\eta_e$, EQE | $(I_{ph}/q)/\phi_{in}$ |
| Internal Quantum Efficiency | $\eta_i$, IQE | $(I_{ph}/q)/\phi_{abs}$ |
| Wall Plug Efficiency (LED) | $\eta$ | $P_{out}/(I_{in} \cdot V)$ |
| Responsivity | $\Re$ | $I_{ph}/P_{opt}$ |
| Specific Detectivity | $D^\star$ | $(S \cdot \Delta f)^{0.5}/\text{NEP}$ |

[a] $I_{ph}$ = Measured photocurrent, $\phi_{in}$ = Incident photon flux, $\phi_{abs}$ = Absorbed photon flux, $P_{opt}$ = Incident optical power, $P_{out}$ = Generated optical power, $I_{in}$ = Input electrical power, $V$ = Applied voltage, $S$ = Device area, $\Delta f$ = Operating bandwidth, NEP = Noise Equivalent Power;

coefficient, $\alpha$, of the material has an important role in the response of the device. Furthermore, transmittance and reflectance are key parameters for transparent electrodes in PDs and LEDs.

Light impinging on a slab of material of thickness $\delta$ is partially reflected at the first surface and partially transmitted in the material. This is then partially reflected at the second surface and partially transmitted outside. In general the transmittance of a free-standing slab of material, $T$, defined as the ratio of the transmitted power ($I_T$) to the incident one ($I_0$), is expressed, in terms of the reflectivity of the two surfaces ($R_1$ and $R_2$), as:[9]

$$T = \frac{I_T}{I_0} = \frac{(1 - R_1)(1 - R_2)\exp(-\alpha\delta)}{1 - R_1 R_2 \exp(-2\alpha\delta)}. \tag{2}$$

The absorption coefficient $\alpha(\lambda)$ is defined as the fraction of power absorbed per unit length into the material, such that the intensity at a distance $x$ in the material is given by: $I(x) = I_0 \exp(-\alpha x)$. Solving eq. (2) for $\alpha$ allows the absorption coefficient to be extracted from the transmittance and reflectance of a material.

For a thin film deposited on a thick substrate, as with TMDs and other 2D crystals, an equivalent formula has been derived by Swanepoel[16]:

$$\alpha = -\frac{1}{\delta}\ln\left(\frac{P + \sqrt{P^2 + 2QT(1 - R_2 R_3)}}{Q}\right), \tag{3}$$

6

where:

$$Q = 2T(R_1 R_2 + R_1 R_3 - 2R_1 R_2 R_3), \tag{4a}$$

$$P = (R_1 - 1)(R_2 - 1)(R_3 - 1), \tag{4b}$$

$$R_1 = \left[\frac{1-n}{1+n}\right]^2, R_2 = \left[\frac{n-s}{n+s}\right]^2, R_3 = \left[\frac{s-1}{s+1}\right]^2. \tag{4c}$$

Here $n$ and $s$ are the refractive indices of the medium and substrate respectively, $R_1$ is the reflectance of the air/medium interface, $R_2$ is the reflectance of the substrate/medium interface and $R_3$ the reflectance of the substrate/air interface. Each $R_i$ can be either measured directly or computed from the knowledge of $n$ and $s$.

Within the non-interacting single particle theory, absorption is related to the optical transitions of electrons from occupied to empty states. The absorption coefficient is zero for photon energies below the bandgap (in absence of mid-gap trap states), it increases sharply for energies close to the bandgap and, in general, stays relatively constant, with the appearance of peaks related to resonant transitions. The band edge has a specific shape:[9,17] for indirect transitions (neglecting excitonic effects) $\alpha \propto (E_{ph} - E_g \pm \hbar\Omega)^m$, where $E_{ph}$ is the incident photon energy, $E_g$ is the bandgap energy, $\hbar\Omega$ is the associated phonon energy and $m$ is equal to 2 for allowed and 3 for forbidden transitions; for direct transitions $\alpha \propto (E_{ph} - E_g)^{0.5}$. Thus, absorption spectroscopy is a viable method to determine the bandgap of a semiconductor and its nature, direct or indirect. In the specific case of 2D materials it has been shown, for example, that the bandgap of few-layer graphene can be tuned with an applied electric field[18] and in TMDs the bandgap energy changes with the number of layers and induced strain.[19] TMDs also show a transition of the bandgap from indirect to direct when they are thinned to single-layers.[3] This large variety of physical phenomena makes absorption spectroscopy an important tool for studying novel, atomically-thin materials.

## I.C   Inelastic light scattering and luminescence spectroscopy

The inelastic scattering of light, or Raman effect, involves the scattering of a photon by an excitation in the examined material.[20] This is usually given by the transition of an electron from the highest occupied molecular orbital (HOMO), or valence band in crystalline solids, into an empty state, which could be a virtual state within the bandgap or a real state above the lowest unoccupied molecular orbital (LUMO) or conduction band. The latter case is referred to as Resonant Raman Scattering (RSS). The excited electron-hole pair then undergoes inelastic scattering with an elemental vibration (phonon) of the material with energy $h\omega_i$, where $i$ designates a particular vibrational band. The frequency shift of the Raman scattering lines is therefore given by $\Delta\nu = \nu_i \pm \omega_i$, where $\nu_i$ is the excitation energy and the minus (plus) sign corresponds to the Stokes (anti-Stokes) process, respectively. In a typical Raman experiment the incoming $(\vec{e_I})$ excitation photon, with energy $h\nu_I$, is provided by a focused laser beam, typically in the visible or near-infrared (NIR) part of the spectrum. Elastically (Rayleigh) and inelastically (Raman) scattered light $(\vec{e_S})$ is then collected and dispersed for wavelength analysis. Selection rules for allowed transitions can be derived using group theory,[20] which determines the symmetry of the vibrational mode. Each phonon mode can be represented by the Raman tensor $\mathbf{R_i}$, for which basis vectors are the crystallographic axes of the crystal (or molecule). The intensity of the Raman signal is given by:

$$I_R = c_1 \sum_i \int \left\| \vec{e_S} \cdot \mathbf{R_i} \cdot \vec{e_I}^{\mathrm{T}} \right\|^2 d\Omega_S, \tag{5}$$

where the integration is carried over the collection angle of the microscope objective $d\Omega_S$, $c_1$ is a material dependent factor and T represents the transpose of the vector. Thus, by changing the excitation and collection axes and the polarization of the light it is possible to determine the crystallographic orientation of the material and identify the different vibrational modes.[21]

The intensity of the Raman scattered light is dependent on the local temperature $T$ and the ratio between Stokes $(I_S)$ and anti-Stokes $(I_{aS})$ intensities can be used as a temperature probe.[22] This has a well-known expression:[23]

$$\frac{I_S}{I_{aS}} = F \cdot C_{ex} \cdot \exp\left(\frac{h\omega_i}{k_B T}\right), \tag{6}$$

where $F$ is a parameter that depends on the optical constants of the material and $C_{ex}$ is a coefficient which accounts for the efficiencies of the optics and gratings at different wavelengths. Since the Raman signal is $\sim 10^6$ times smaller than the Rayleigh process, a very narrow notch filter, centred at the excitation wavelength, is typically used to reject the unwanted signal.

Radiative transitions of electrons from an excited state to a lower level lead to the emission of light, a process known as luminescence.[9] These transitions can be initiated by the absorption of a photon, known as Photoluminescence (PL), fluorescence and phosphorescence, or by the application of an electric field through the material, known as Electroluminescence (EL). In both cases, detailed measurement of the spectral intensity of the emitted light can give insight into the properties of the material and the performance of the examined device. In a typical PL experiment the excitation source is a laser, with a wavelength appropriate for exciting resonant electronic transitions. The emitted light from the material is then dispersed for spectral analysis. Usually a low-pass filter is used to reject the excitation wavelength. The detailed physical processes involved in PL are linked to the excitation and decay probabilities in the material.[9] The frequency-dependent intensity of a luminescence process can be written, in general, as:

$$I_L(h\nu) \propto \|M\|^2 \cdot g(h\nu) \cdot \Gamma_e, \tag{7}$$

where $\|M\|^2$ is the matrix element of the transition, $g(h\nu)$ is the density of states (DOS) and $\Gamma_e$ represents the occupancy factors for the transition, which are related to the probability of the upper (lower) levels to be empty (occupied).

# II  Instrumentation

## II.A  Optics

Figure 1 shows a schematic of the optical and electrical components of the system whilst a 3D model presenting the actual implementation of the components is shown in fig. 2. A set of visible wavelength CW diode lasers (*Coherent* OBIS 375LX, 473LS, 514LX, 561LS and *Omicron* LuxX 685, with powers ranging from 30 to 50 mW) is fitted in an enclosure system, which facilitates the alignment of each laser and can host up to 6 different wavelengths. Each laser is digitally modulated and the power is adjusted using an analog signal. Continuous modulation and TTL operation can be achieved by use of a digitally-controlled signal generator. Careful choice of dichroic mirrors inside the laser enclosure allows multiple wavelengths to be used at the same time. The laser light is then delivered with a series of kinematic and fixed mirrors into the illumination path of the optical microscope (*Olympus* BX51), see blue shaded area in fig. 1, after a ×3 beam expansion. A dichroic beam splitter (BS) is used to direct the light in the custom built epi-illumination section of the microscope. A rotatable (360°) achromatic $\lambda/2$ waveplate (*ThorLabs* AHWP05M-600) is used to rotate the polarization of the laser light. A custom-built drop-in-filter (DiF) system is used to introduce neutral density (ND), polarisers, notch and band-pass filters in the optical path of the lasers and the microscope: the same filter holders and housings are used throughout the system, ensuring full compatibility in each section. Invisible (UV) laser light is fed into the microscopy directly from the epi-illumination BS cubes after a ×3 beam expansion to secure a superior laser beam resolution delivered to the sample.

White light for reflection microscopy is provided by a white LED along the optical path of the laser beams, while transmittance illumination is achieved using the microscope's built-in lamp and condenser lens. Both the white and laser light are directed to the objective using either a 50%/50% BS or the appropriate dichroic band-pass (BP) mirror. The reflected light collected by the objective is directed to a CCD imaging camera or, by using a flip mirror (FM), to the entrance slit of the spectrometer. The microscope is fitted with *Olympus* MPLanFL-N Semi-Apochromat infinity-corrected lenses with ×5, ×10, ×20 and ×50 magnification.

The spectroscopy section is composed by a focusing achromatic lens (*ThorLabs* AC254-150-A) with x/y and focus adjustment. The spectrometer is a *Princeton Instruments* Acton SP2500, equipped with three dispersion gratings (1200 g/mm with 500 nm and 750 nm blaze, and 1800 g/mm with 500 nm blaze) and a *Princeton Instruments* PIXIS400-eXcelon back-illuminated, peltier cooled, CCD camera. In our multi-purpose instrument, each grating is used for different measurements as they differ by number of grooves and blaze wavelength (at which the efficiency is at maximum and the same for both S and P polarizations). In white light spectroscopy applications, corrections to account for the optics and gratings efficiencies, at different wavelengths, can be applied using *Princeton Instruments* IntelliCal system.

The microscope stage is a *Prior Scientific* OptiScan ES111 with ProScan III controller. The minimum step size is 10 nm. Focus control is also achieved trough the same controller.

The whole system is built on a vibration-isolated $120 \times 90 \, \text{cm}^2$ optical table. The laser light delivery system is enclosed within *ThorLabs* stackable tube lens system, allowing a light-tight connection. The microscope stage, foot and objective turret is covered with a light-tight enclosure, formed by a metal frame and a conductive fabric curtain connected to the ground of the electrical circuit to ensure shielding from electro-magnetic noise. The front of the curtain can be lifted to allow access to the stage and it is fitted with laser interlocks. The light-tight delivery system and enclosure, together with the magnetic interlocks, make the system a Class 1 laser product. The same light-tight tubes are used also to deliver light to the spectrometer, enabling the use of our instrument without the need of a darkened room.

The custom-built epi-illumination system allows flexible and quick configuration of the microscope for different measurements. As shown in fig. 3, the optical path can be configured for scattering, transmission/reflection spectroscopy and laser light illumination (as in SPCM) simply by replacing or removing the appropriate filters and BS. Each BS unit is fitted with magnetic interlocks for safety purposes. Figure 3a shows the configuration for reflectance measurements: light from the white LED travels freely (no laser BS fitted) after being collimated and reaches the objective though a 50%/50% BS; reflected light is collected by the same objective and partially transmitted by the BS to a FM which directs it into the spectrometer. A similar arrangement is

used for transmittance spectroscopy, as shown in fig. 3b. In this case the BS is replaced with a mirror and the white light from the incandescent bulb is collimated by the microscope condenser and, after travelling in the sample, collected by the objective and directed to the spectrometer. Figure 3c shows the configuration for laser-light illumination and SPCM: in this case a dichroic BS is used to direct the laser light into the objective and the reflected light is partially transmitted to the imaging camera for direct assessment and focussing; the LED can be used at the same time for imaging. The configuration for Raman and luminescence spectroscopy is shown in fig. 3d: in this case the scattered light is collected by the objective and directed to the spectrometer via the FM, a notch filter is used to remove the Rayleigh component while ND and laser-line filters can be used to attenuate the beam power and clean it from spurious wavelengths. The latter two configurations can be used at the same time to perform Raman or PL mapping together with SPCM. Polarized Raman spectroscopy can be performed by interposing a polarizing filter (analyser) between the notch filter and the spectrometer, while the laser polarization is controlled by the $\lambda/2$ waveplate.

A photodetector (PD) mounted on the stage, see fig. 1, is used to automatically record the power of the laser light after a measurement, by programming the stage and the acquisition software accordingly. The ability to modulate the power of the lasers, both electrically and by introducing ND filters along the beam path, allows the system to span a power range (with the $\times 50$ objective) between $\sim 2$ nW and $\sim 20$ mW in steps of $0.4 \cdot 10^{-OD}$ mW, where $OD$ is the optical density.

Design of optical systems involving lasers rely strongly on the knowledge of the shape and size of the beams. In our setup, solid-state diode lasers are used and all the optical components are chosen so that to minimize deviations from the $TEM_{00}$ laser mode, which has a Gaussian intensity distribution:

$$I(r, r_b) = \sqrt{\frac{2}{\pi}} \frac{1}{r_b} \exp\left(-\frac{r^2}{r_b^2}\right), \tag{8}$$

where $r$ is the distance from the optical axis and $r_b$ is the radius of the beam, measured at the point at which the beam intensity falls by 50% (FWHM). As the beam is transmitted through a circular aperture of radius $r_a$, such as the pupil aperture of the objective lens, the transferred power is:

$$P_b = 1 - \exp\left(-\frac{2r_a^2}{r_b^2}\right) = 1 - \exp\left(-\frac{2}{T^2}\right), \tag{9}$$

where $T = r_b/r_a$ is defined as the Gaussian beam truncation ratio. The focused beam profile is Gaussian for $T < 0.5$ and converges to the Airy pattern for $T \to \infty$. The focused spot size diameter ($d_s$) can be expressed as:[24,25]

$$d_s = \frac{K\lambda}{2\text{NA}}, \tag{10}$$

where NA is the numerical aperture of the lens, $\lambda$ is the wavelength of the laser and $K$ is the $k$-factor for truncated Gaussian beams, which is a function of $T$ only. Urey[24] computed approximate expressions for $K$ for the two cases $T < 0.5$ (Gaussian) and $T > 0.4$ (Truncated Gaussian). In the same work an expression to determine the depth of focus, $\Delta z$ (i.e. the distance along the optical axis at which the irradiance drops by 50%), was determined:

$$\Delta z = K_2 \lambda f_\#^2, \tag{11}$$

where $f_\#$ is the ratio between the clear aperture diameter and the focal length of the lens (also called $f$-number) and $K_2$ is the focus $k$-factor, again a function of $T$ only. In our apparatus we found that $T = 1.03$ for the UV (375 nm) laser and $T = 0.52$ for the visible lasers when using the $\times 50$ objective. In table 2 we show the results obtained for our system using equations 10, 11 and the results in Ref. Urey[24]. The calculated values show that our system is able to focus the laser light well in the diffraction-limit of the objective lens, allowing ultra-high spatial resolution. The very narrow depth of focus allows substrate contributions to be minimized.

Table 2: Laser spot diameters and depth of focus of the lasers in our apparatus with the $\times 50$ objective.

| $\lambda$ (nm) | $d_s$ (nm) | $\Delta z$ (nm) |
|---|---|---|
| 375 | 264 | 158 |
| 473 | 445 | 268 |
| 514 | 484 | 291 |
| 561 | 528 | 320 |
| 685 | 645 | 390 |

## II.B   Electronics

Optoelectronic devices based on graphene and 2D materials are usually fabricated from thin flakes deposited on a Si substrate capped with a $SiO_2$ layer, where electrical contacts are defined via lithography and metal evaporation. We designed a chip carrier for our microscope which allows versatile and easy connection of such devices. As shown in fig. 4, the carrier is composed of a PCB board ($34 \times 29 \, mm^2$) with two standard 11-way pin strips, where 20 of these pins are connected to gold-coated pads and one to a central $15 \times 15 \, mm^2$ gold-coated pad (one is not connected). The central pad is used to contact, using silver paint, the doped silicon substrate which provides electrostatic gating. The other pads are used to connect the device's pads to the PCB board using wire bonding. The design of the chip carrier differs from standard, commercially available, boards since the sample is not buried in a plastic or ceramic case, it is, instead, above the PCB and the soldering pads. In this way the objective lens cannot come into contact with parts of the chip carrier and long-working distance lenses are not required, thus improving the maximum achievable spatial resolution and minimum laser spot size. The chip carriers can also be fabricated with a central aperture, as shown in fig. 4b, allowing transmitted light to be used to characterize devices fabricated on transparent substrates.

Thanks to the standard single-in-line package (SIP) pins, the chip carriers are connected to female sockets on a second PCB board which is anchored on the microscope stage. This board is then connected though a shielded multi-core cable to a breakout BNC box, which enables connections with different measuring instruments, such as lock-in amplifiers, voltage/current amplifiers and multimeters, as shown in figures 1 and 2. In order to screen the devices from external electric fields, the light-tight enclosure surrounding the stage is made of conductive fabric and connected to the ground of the circuit, together with the walls of the BNC box. All measuring instruments are decoupled from the rest of the electric instruments *via* insulating transformers, while signal and bus lines are kept isolated from the measuring PC *via* opto-electronic decouplers (*National Instruments* GPIB-120B).

Full automation of the system is achieved with a custom-made LabView-based software which is able to communicate to all electronic instruments via GPIB/USB bus and modulate the lasers

*via* digital-to-analog interface (DAC) (*National Instruments* NI-DAQ); Native software is used to control the spectrometer and CCD camera, interfaced with the same LabView software.

# III  Performance of multi-purpose microscope system

## III.A  Optoelectronic devices

As an example of the ability of our setup to perform characterization of optoelectronic devices, we present typical measurements performed on a graphene-based photodetector. The apparatus is setup as in fig. 3c, where the WL source is used for imaging purposes and switched off during the measurements. The device is comprised of a single-layer exfoliated graphene flake, contacted in a two-terminal geometry with Cr/Au contacts, on a Si substrate capped with $SiO_2$ gate oxide, see fig. 5a, left panel. Details on the fabrication and properties of such devices are beyond the scope of this paper and discussed elsewhere in the literature.[12,14,26,27] In fig. 5a, right panel, we show the SPCM map of such device acquired with a 473 nm laser (24 kW/cm$^2$ incident power) in steps of $0.5\,\mu$m, under a source-drain bias $V_{SD} = 10$ mV and back-gate voltage $V_{BG} = 0$ V. The map shows strong photocurrent at the graphene/metal interface, in agreement with previous reports.[12,27] We then characterize the electronic response of the device directly on the microscope stage. Figure 5b shows the back-gate sweep (typical for a graphene FET) of the device under the same $V_{SD}$: from this we can extrapolate several parameters, such as the level of doping (holes in this case) $n \simeq 2.1 \cdot 10^{12}$ cm$^2$ and the field-effect hole mobility $\mu_h \simeq 650$ cm$^2$V$^{-1}$s$^{-1}$. All measurements are performed using a *DL* Model 1211 current amplifier, an *Ametek* 7270 DSP lock-in amplifier and a *Keithley* 2400 SourceMeter to provide the source and gate biases.

As a further system characterization, we demonstrate the polarization capabilities of our apparatus by measuring the polarization dependence of the observed photocurrent. We focus the laser at the graphene/metal interface and rotate the $\lambda/2$ waveplate, in order to change the polarization of the incident light, while recording the photocurrent. It is well known that, in this type of device, hot-carriers dynamics in graphene, combined with the direct absorption of the metal contacts, lead to a polarization-dependent photocurrent.[27] In fig. 5c we show a plot of the photocurrent as a func-

tion of polarization angle $\theta$. We observe that $I_{ph}$ is maximum when the polarization is orthogonal ($\perp$) to the metal contact and minimum when it is parallel ($\parallel$) to it, as expected.[27] The angle $\theta$ is defined as the angle between the polarization of the laser and the vertical (y) axis of the microscope stage. Since our device sits at an angle $\phi \simeq 57°$ with respect to y (see fig. 5a), the polarization dependence should have a "phase shift" of the same amount, i.e. $I_{ph} \propto \sin(2(\theta - \phi))$, as verified in fig. 5c (solid blue line).

## III.B  Absorption spectroscopy

In section I.B we showed that, in order to extrapolate the absorption coefficient of a material, we need to perform transmittance and reflectance measurements. These can be done in our system by using the optical configurations shown in fig. 3a-b. As a characterization of the performance of our setup we present a series of measurements of transmittance and absorption coefficient for different materials.

Figure 6a shows the visible transmittance of single-layer and multi-layer CVD-grown graphene. As expected,[28] single layer graphene shows a flat transmittance $\sim 97.7\%$ across the whole visible spectrum, while nickel-grown multi-layer CVD graphene[29] shows a transmittance of $\sim 75 - 80\%$. The contribution of the transparent substrate, quartz in this case, has been subtracted from the data by performing a calibration measurements on a bare substrate.

We now show two examples of absorption coefficient measurements, performed by measuring transmittance and reflectance and applying eq. (3). The first example is a thin layer of organic crystalline semiconductor, Rubrene. The optical and electrical properties of this organic semiconductor have been intensively studied.[30] Therefore, it offers a good standard test the performance of the developed multi-purpose microscope system. Figure 6b shows the measured $\alpha(\lambda)$ of a Rubrene crystal on glass, using unpolarized light, perpendicular to the a-b facets and parallel to the c facet of the crystal (see Ref. Irkhin et al.[30] for details). The measured spectrum is in very good agreement with literature, both in the intensity and position of the peaks.[30] As a second demonstration of the spectroscopy capabilities of our system, we measured the absorption coefficient of ultra-thin HfS$_2$. This is a well known TMD which was well characterized in the past as a bulk crystal[31] and

recently as a thin flake on a substrate. Figure 6c, inset, shows the absorption coefficient of a $\sim 25$ nm thick flake of freshly-exfoliated $HfS_2$. The values agree well with literature.[17,31] Owing to the proportionality between $\alpha$ and $E$ (see section I.B), we are able to extrapolate the bandgap of the material by plotting $\alpha^2$ as a function of $E$. The intercept of the extrapolated linear part mark the direct bandgap of the material $E_g = 2.75 \pm 0.01$ eV, in very good agreement with established values.[31]

## III.C  Raman spectroscopy

To demonstrate the ability of our set-up to also perform inelastic light spectroscopy we characterized it by studying two well-known materials: Si and graphene. Figure 7a shows the Raman spectrum of commercial-grade Si, acquired with $\lambda_{\text{exc}} = 514$ nm at 1.0 MW/cm$^2$ incident power for 10 s, where the first-order transverse-optical phonon (1TO) mode mode at $\sim 520\,\text{cm}^{-1}$ is captured in both Stokes (negative shift) and anti-Stokes (positive shift) regime in a single snapshot. The FWHM ($\Gamma$) of the Rayleigh line ($0\,\text{cm}^{-1}$) is only $7\,\text{cm}^{-1}$, and the Lorentzian fit of the Si modes gives $\Gamma = 17\,\text{cm}^{-1}$. Using eq. (6) for $T = 291$ K and $F = 0.97$ (see Ref. Jellison et al.[23] for details), we find an expected value of $I_S/I_{aS} = 11.92$; the experimental value extrapolated from fig. 7a is $I_S/I_{aS} = 22 \pm 2$, giving an experimental correction factor $C_{ex} \simeq 1.84$. In the following discussion we will adopt the common convention for which the Stokes lines are reported with positive shift, instead of negative.

Characterization of graphene and other 2D material relies strongly on Raman spectroscopy.[8] The resonant Raman spectrum, acquired with our setup, of exfoliated graphene is shown in fig. 7b. We observe the G peak at $\sim 1580\,\text{cm}^{-1}$, originating from the $E_{2g}$ mode and the double-resonant 2D band at $\sim 2680\,\text{cm}^{-1}$, originating from the $A_{1g}$ mode. The 2D band is sensitive to the number of layers: it is given by a single Lorentzian peak for single-layer graphene, the convolution of four Lorentzian peaks for bi-layer graphene and the convolution of six peaks for tri-layer graphene.[32] In fig. 7b we show the ability of our system to resolve such multi-peak structures (green lines) and thus discriminate the number of layers in graphene flakes. Figure 7c shows the same spectrum of single-layer graphene acquired at different incident powers. The inset shows the height of the G

peak as a function of incident power, adhering to the expected linear relationship. This serves to confirm that no artefacts are introduced in the spectra by the experimental apparatus. It is worth noting that we are able to resolve clearly the G and 2D bands with an incident power density as low as 50 kW/cm$^2$ with an acquisition time of only 2 s for the whole spectral range.

In our setup it is possible to perform polarized Raman spectroscopy using the configuration shown in fig. 3d. This technique has recently been applied to the investigation of graphene[33] and TMDs,[34] where strong polarization dependence is given by valley anisotropy, highlighting the role of Raman spectroscopy in the study of electron-phonon coupling. To demonstrate the polarization capabilities of our setup, we characterized the dependence of the Raman modes of Si upon incident polarization. Figure 8a shows the Raman spectrum of Si with the [100]-surface perpendicular to both the incident and the scattered light ($zxx\overline{z}$ and $zxy\overline{z}$ configurations), acquired with $\lambda_{\mathrm{exc}} = 514$ nm at 2.1 MW/cm$^2$ incident power for 2 s. We observe the 1TO mode at $520\,\mathrm{cm}^{-1}$ and a two-phonon mode at $\sim 900 - 1000\,\mathrm{cm}^{-1}$. Using eq. (5) and the expression for the Raman tensor of the 1TO mode, we find that the Raman intensity of this mode is given by:[21]

$$I_R(\vartheta, \varphi) = c_2 \sin^2(\vartheta - 2\varphi), \tag{12}$$

where $\vartheta$ is the polarization angle between the incident and scattered light. As the angle between the incident polarization and the [100] axis $\varphi$ is varied, we observe a decrease of the 1TO peak, while the two-phonon mode changes only slightly, as shown in fig. 8a. Equation (12) is verified in fig. 8b-c where the intensity of the 1TO mode is plotted as a function of $\vartheta$ and $\varphi$, respectively. The angle $\varphi$ is varied by rotating the polarization of the laser with a $\lambda/2$ waveplate, while the angle $\vartheta$ is defined by the angle of the analyser with respect to the waveplate (see fig. 4d). In this way there is no need to rotate the sample, making it possible to have electrical connections to the devices. At the same time, this technique can be used to asses the orientation of the sample, since a measurement of the $\vartheta$ dependence will give a value of $\varphi \neq 0$ if the [100] axis is not aligned with the incident polarization angle.

## III.D    Luminescence spectroscopy

In this section we characterize the ability of our system to measure luminescence phenomena: photoluminescence (PL) and electroluminescence (EL). As an example of a PL measurement we use single-layer $WS_2$, a semiconducting TMD with good potential in optoelectronic applications.[35,36] The room-temperature PL spectrum is shown in fig. 9a. This is acquired using the configuration shown in fig. 3d, with $\lambda_{\mathrm{exc}} = 514$ nm, $P = 5.1$ kW/cm$^2$ and 10 s acquisition time; the power is kept low to avoid causing damage to the sample. A strong peak is observed, centred at 2.02 eV and the Raman modes can be also observed in the same spectrum (highlighted in the green box). Fit with Lorentzian curves of the Raman modes (inset) gives the following values: $2LA(M) = 353\,\mathrm{cm}^{-1}$, $A_{1g}(\Gamma) = 420\,\mathrm{cm}^{-1}$, $A_{1g}(M) + LA = 585\,\mathrm{cm}^{-1}$ and $4LA(M) = 705\,\mathrm{cm}^{-1}$. Both the PL and Raman spectra are in perfect agreement with commonly accepted values.[37]

As an example of EL device characterization, we use a $ZnS_2$-based ACEL device with both graphene and functionalized graphene transparent electrodes.[38] Figure 9b shows the spectral emission of such device with graphene and $FeCl_3$-intercalated graphene electrodes. The spectra can be decomposed into multiple Gaussian peaks, corresponding to the intraband transitions[39] in $ZnS_2$. The use of our instrument allows the accurate comparison of the two electrode materials and the performance of the different devices (see Torres Alonso et al.[38] for details).

# IV    Conclusion

We have presented the design of a new multi-purpose instrument for the characterization of optoelectronic devices based on 2D materials, capable of performing multiple electrical and optical measurements simultaneously. We demonstrated the performance of the setup with a series of techniques, involving a multitude of materials, showing results at the level of the state-of-the-art commercial equipment. The ability to perform low-frequency electrical transport measurements, SPCM, Raman, absorption and PL spectroscopy, combined with full automation, high sensitivity and low noise, make our instrument ideal to face the challenges imposed by the advent of atomically-thin materials in optoelectronic devices.

Customization of each section allows multiple routes for future upgrades and expansion, these will include: a vacuum chamber microscope stage with temperature control, multi-wavelength Raman spectroscopy, auto-focusing and high-frequency (RF) measurements. The cost and size is very contained, making it suitable for small laboratories and the safety features introduced make it very easy to operate, with minimal training required.

**Author contributions** All authors contributed to the design of the system. A.D.S. assembled the instrument, performed the characterization measurements, prepared the schematic figures and wrote the manuscript, with contributions from all authors. G.F.J. and N.J.T. designed the PCB sample-holders and provided advice on the design. G.F.J. provided the Rubrene and $WS_2$ samples and analysed the absorption measurements. M.F.C. and S.R. supervised the project and provided advice on the measurements and the manuscript.

**Competing financial interests** The authors declare no competing financial interests.
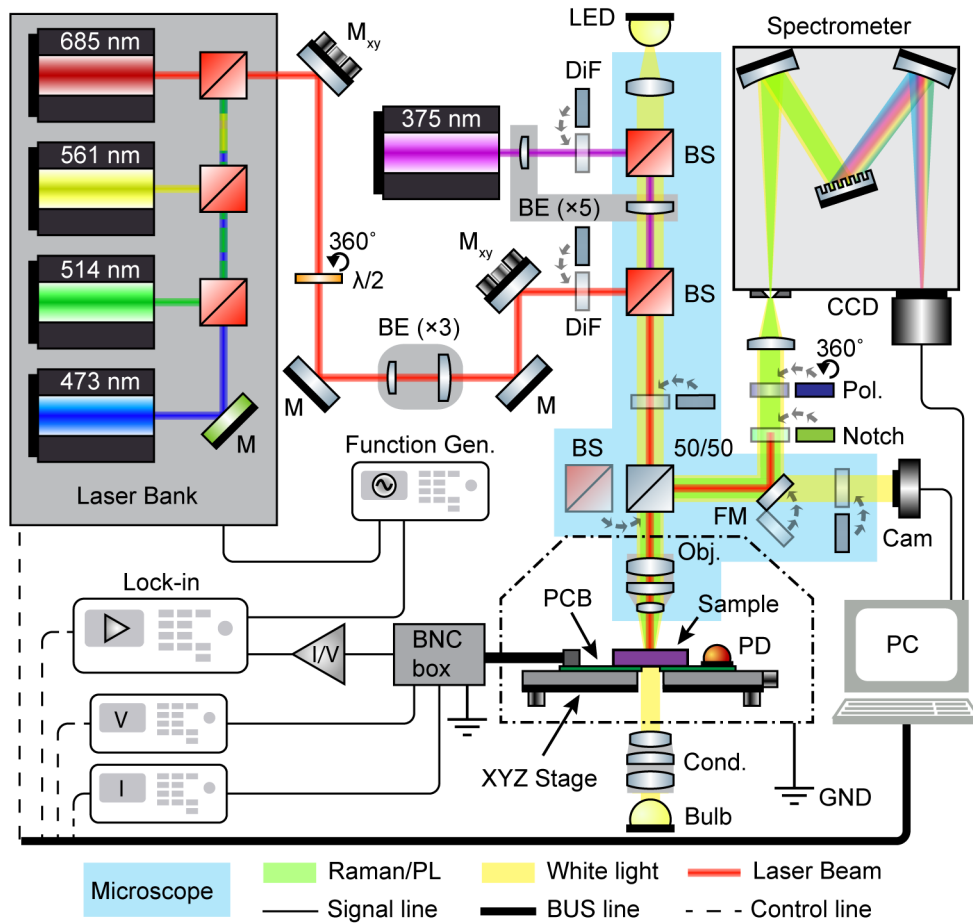
Figure 1: **Schematic of the optoelectronic setup.** Laser light is used for scanning photocurrent mapping, Raman and Photoluminescence (PL) spectroscopy. Four CW diode lasers are fitted in a laser enclosure while the UV laser source is directly attached to the microscope. White light from two different sources can be used for transmittance and reflectance measurements. An XYZ motorized microscope stage allows precise control of the sample position. The dash-dotted line represents the electrically screened light-tight enclosure of the sample stage. Signal lines carry electric/data signals to be measured, control lines carry the signals to configure the instruments, the lasers and the other sources, BUS line comprises USB and GPIB. Abbreviations: mirror (M), kinematic mirror ($M_{xy}$), half-wavelength plate ($\lambda/2$), beam expander (BE, followed by magnification), drop-in filter (DiF), beam splitter (BS, dichroic in red), Polariser/Analyser (Pol.), white light (WL), voltage (V) or current (I) sources/meters, flip mirror (FM), sample holder (PCB), photodetector (PD), condenser (Cond), microscope objective (Obj), imaging camera (Cam), spectroscopy camera (CCD), ground line (GND). Created with ComponentLibrary[40] symbols.
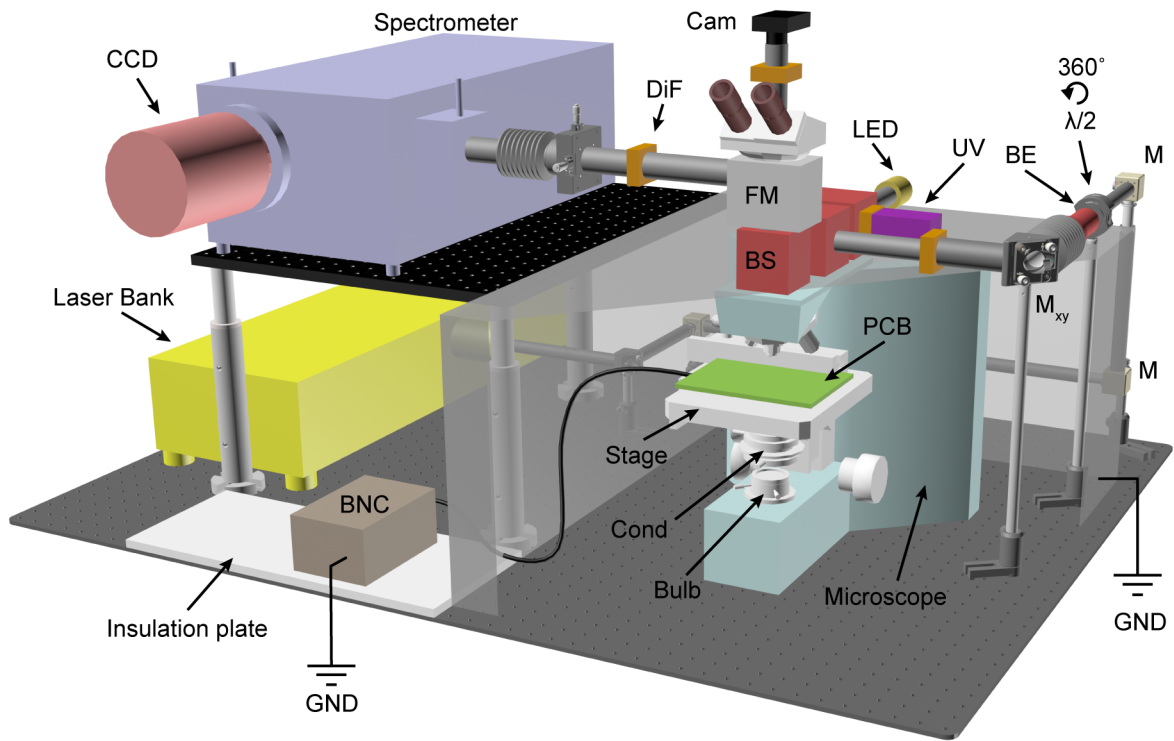
Figure 2: **3D model showing the implementation of the setup.** The system is built on a vibration-isolated optical table ($120 \times 90$ cm$^2$). Four main components can be identified: upright microscope with custom-built EPI illumination system and motorized XYZ stage; Custom-built laser-enclosure; Spectrometer and CCD camera; Sample-holder PCB board with BNC break-out box. The electrically screened, light-tight, enclosure of the sample is shown in transparency and sectioned, this is directly grounded. Tube lenses are used to cover the light path of the laser beams, magnetic interlocks are located in the screen enclosure and in the BS cubes, effectively making the system a Class 1 laser product. Labels and abbreviations as in Figure 1.
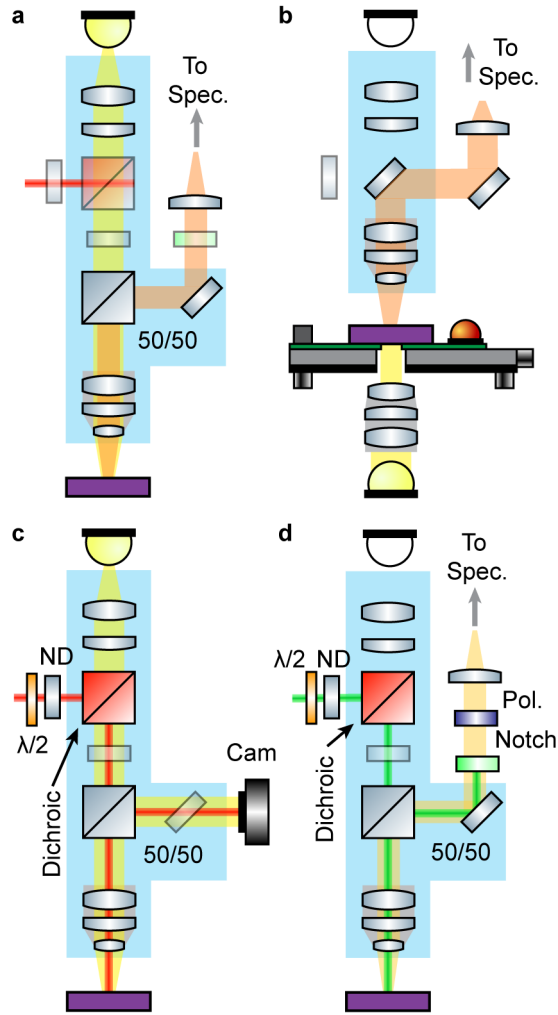
Figure 3: **Flexible Optical path configurations.** **a**, Reflectivity and **b**, Transmittance measurements using white light. **c**, Scanning photocurrent mapping with laser light; **d**, Raman/Fluorescence/Photoluminescence spectroscopy, including polarization. **c** and **d** can be combined and performed at the same time. UV laser delivery system is omitted. Symbols and abbreviations as in Figure 1.
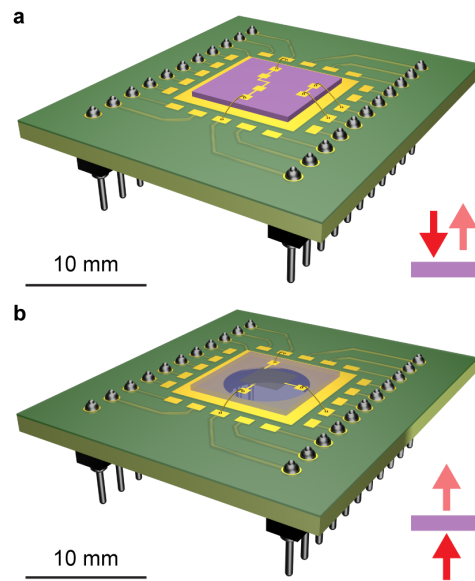
Figure 4: **Custom PCB chip-carrier boards.** **a**, Opaque substrates configuration where reflected and laser light is used. **b**, Transparent substrate configuration where transmitted light is used. Yellow areas are gold-coated pads. Scale bars are 10 mm
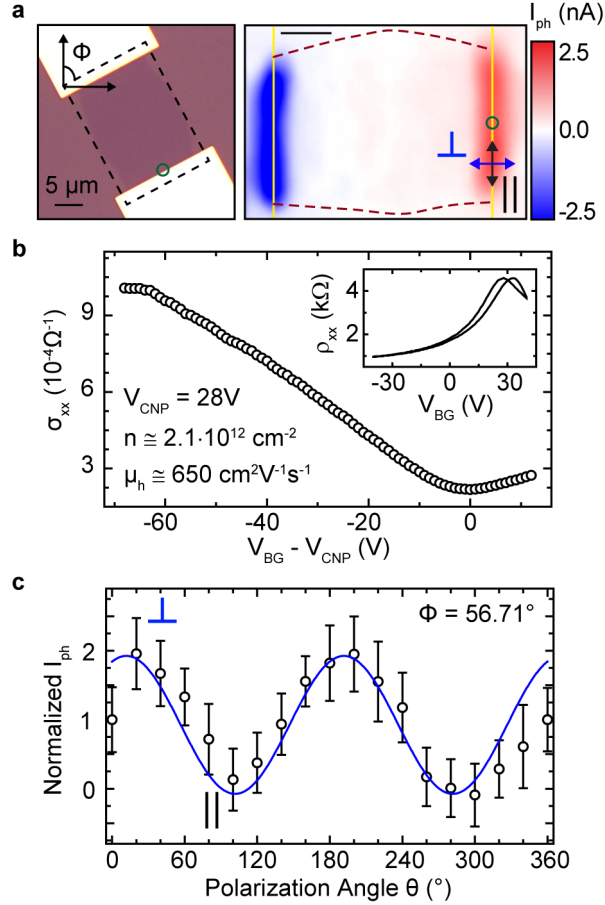
Figure 5: **Characterization of a graphene-based PD. a**, Optical micrograph of the single-layer graphene device in FET configuration (left) and SPCM map at $\lambda_{\mathrm{exc}} = 473$ nm acquired with our microscope (right); black-dashed box marks the mapped area, red-dashed lines mark the graphene flake boundary. Scale bars are $5\,\mu$m. **b**, Electrical characterization of the graphene FET, acquired in the same setup, showing the conductivity as a function of back-gate voltage. **c**, Polarization dependence of the observed photocurrent $I_{ph}$ at the graphene-metal contact (green circle in panel **a**), maximum photocurrent is observed for light polarized $\perp$ to the metal contact. $\phi$ marks the angle between the vertical (y) axis of the microscope stage ($\theta = 0°$) and the graphene-metal interface, solid blue line is the expected dependence (see main text).
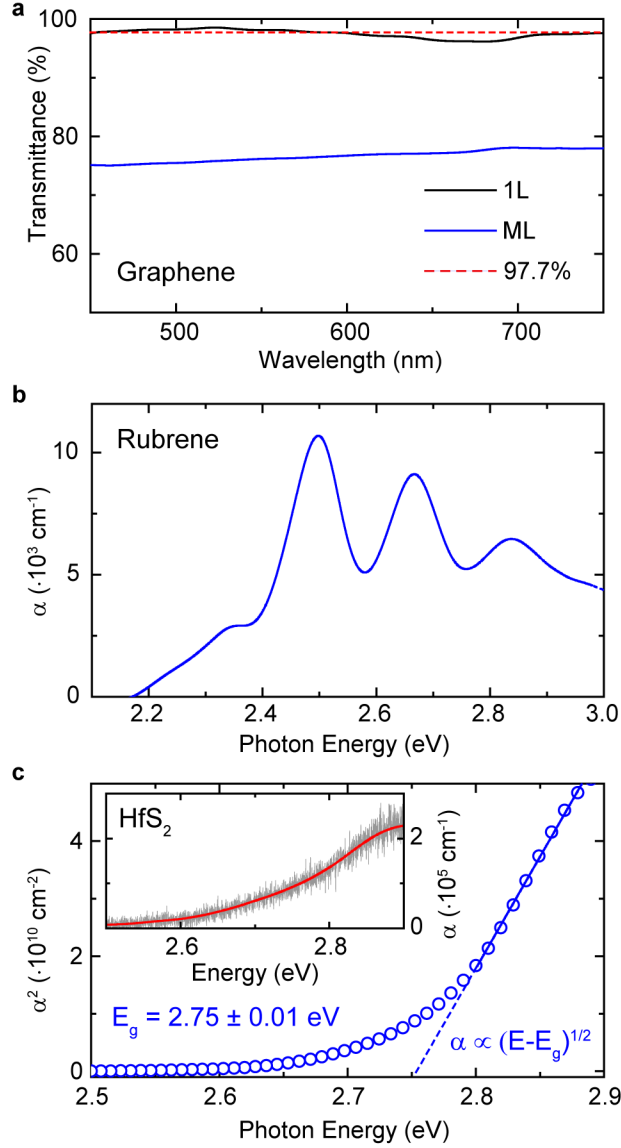
26

Figure 6: **Absorption spectroscopy characterization. a**, Visible transmittance of CVD-grown single- (1L) and multi-layer (ML) graphene, dashed line marks the theoretical 97.7% transmittance of single-layer graphene; **b** Unpolarized absorption coefficient $\alpha$ of a Rubrene crystal, measured perpendicular to the ab facet; **c**, Absorption coefficient $\alpha$ of ultra-thin ($\sim 25$ nm) $HfS_2$ and direct-gap determination, $E_g = 2.75 \pm 0.01$ eV.
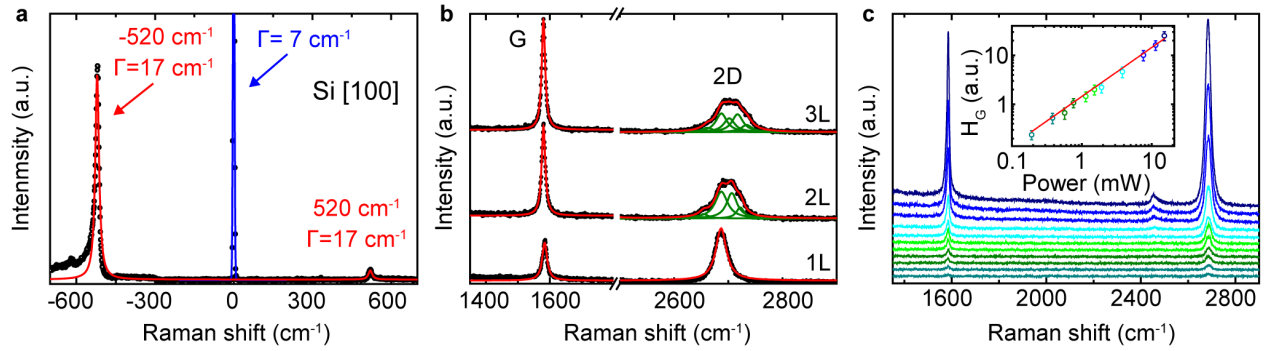
Figure 7: **Raman spectroscopy characterization.** **a**, Stokes and anti-Stokes bands of Si [100] at room temperature; **b**, Resonant Raman spectra of single- (1L), bi- (2L) and tri- (3L) layer graphene, red solid lines are cumulative fit to Lorentzian curves (shown in green); **c**, Raman spectrum of single-layer graphene as a function of incident optical power and power-dependence of the G-peak heigh (inset), solid line marks a slope of 1, curves shifted for clarity. All spectra are acquired with $\lambda_{\text{exc}} = 514$ nm at 2.1 MW/cm$^2$ incident power and 2 s acquisition time.
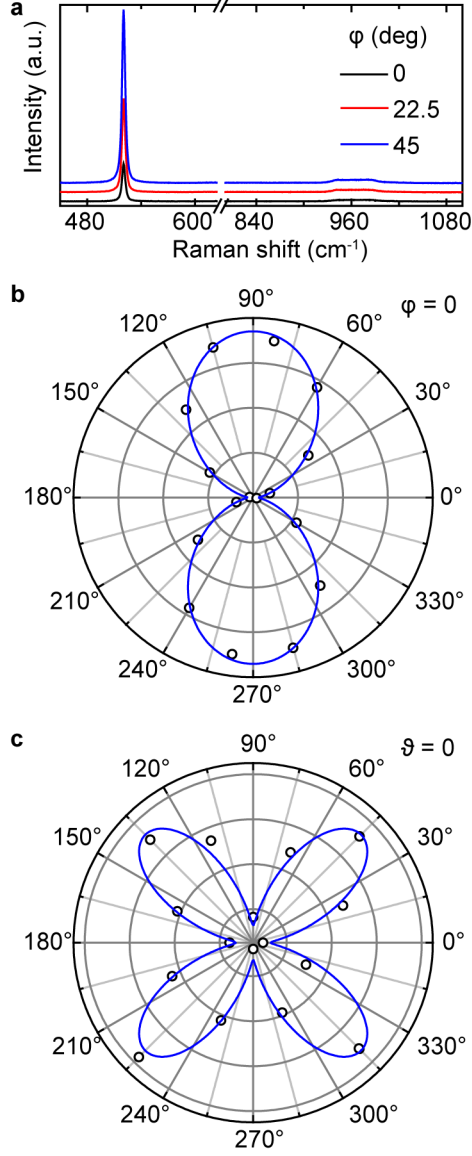
Figure 8: **Polarized Raman spectra of Si [100]. a**, Raman spectra of Si showing the first-order (TO)-phonon mode of Si at $\sim 520\,\mathrm{cm}^{-1}$ and two-phonon mode at $\sim 900-1000\,\mathrm{cm}^{-1}$. **b**, Polar plot of the height of the (TO)-phonon mode as a function of the angle between polarization directions $\vartheta$ ($\varphi = 0$) and **c**, same plot as a function the rotation angle about the [100] axis $\varphi$ ($\vartheta = 0$), solid line is given by eq. (12). $\lambda_{\mathrm{exc}} = 514$ nm, $P_{\mathrm{opt}} = 1.2$ MW/cm$^2$, 2 s acquisition time.
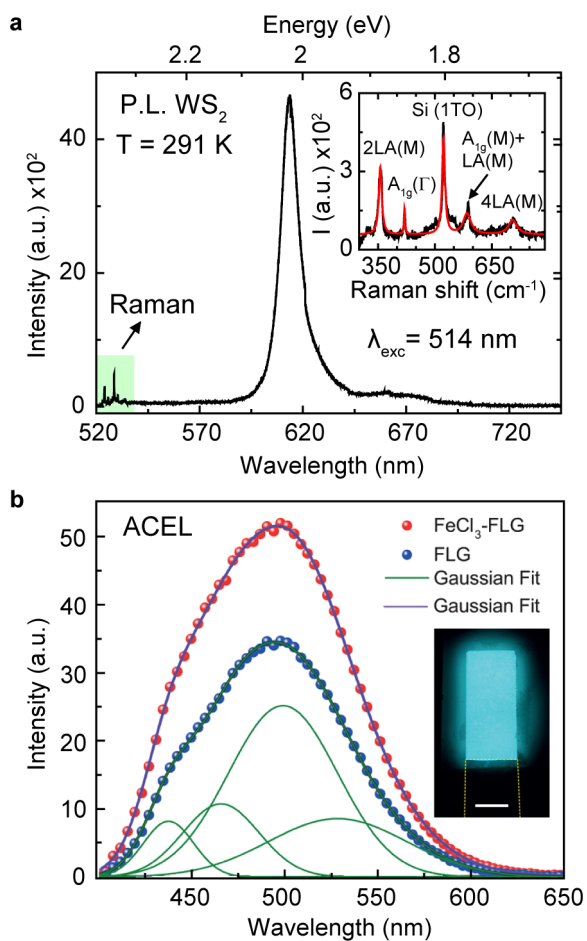
Figure 9: **PL spectroscopy and EL devices characterization. a**, Room temperature Photoluminescence of CVD-grown single-layer $WS_2$, $\lambda_{exc} = 514$ nm, $P = 5.1$ kW/cm$^2$, 10 s acquisition time. Inset: zoom on observed Raman modes. **b**, $ZnS_2$-based ACEL device spectral emission: comparison between few-layer graphene and $FeCl_3$-intercalated graphene electrodes. Inset: picture of the working device. Scale bar is 1 cm. Adapted with permission from Torres Alonso et al. [38] © 2016 American Chemical Society.

# References

(1) Geim, A. K.; Novoselov, K. S. The rise of graphene. *Nat Mater* **2007**, *6*, 183–191.

(2) Geim, A. K. Graphene: Status and Prospects. *Science* **2009**, *324*, 1530–1534.

(3) Wang, Q. H.; Kalantar-Zadeh, K.; Kis, A.; Coleman, J. N.; Strano, M. S. Electronics and optoelectronics of two-dimensional transition metal dichalcogenides. *Nat Nano* **2012**, *7*, 699–712.

(4) Chhowalla, M.; Shin, H. S.; Eda, G.; Li, L.-J.; Loh, K. P.; Zhang, H. The chemistry of two-dimensional layered transition metal dichalcogenide nanosheets. *Nat Chem* **2013**, *5*, 263–275.

(5) Pospischil, A.; Mueller, T. Optoelectronic Devices Based on Atomically Thin Transition Metal Dichalcogenides. *Applied Sciences* **2016**, *6*, 78.

(6) Cho, A.-J.; Park, K. C.; Kwon, J.-Y. A high-performance complementary inverter based on transition metal dichalcogenide field-effect transistors. *Nanoscale Res Lett* **2015**, *10*, 115, 25852410.

(7) Tan, C.; Liu, Z.; Huang, W.; Zhang, H. Non-volatile resistive memory devices based on solution-processed ultrathin two-dimensional nanomaterials. *Chem. Soc. Rev.* **2015**, *44*, 2615–2628.

(8) Ferrari, A. C.; Basko, D. M. Raman spectroscopy as a versatile tool for studying the properties of graphene. *Nat Nano* **2013**, *8*, 235–246.

(9) Fox, M. *Optical Properties of Solids*; Oxford University Press, 2010.

(10) Wilson, J.; Hawkes, J. F. B. *Optoelectronics: An introduction*; Prentice-Hall, 1942.

(11) Bredol, M.; Schulze Dieckhoff, H. Materials for Powder-Based AC-Electroluminescence. *Materials* **2010**, *3*, 1353.

(12) Koppens, F. H. L.; Mueller, T.; Avouris, P.; Ferrari, A. C.; Vitiello, M. S.; Polini, M. Photodetectors based on graphene, other two-dimensional materials and hybrid systems. *Nat Nano* **2014**, *9*, 780–793.

(13) Graham, R.; Yu, D. Sanning photocurrent microscopy in semiconductor nanostructures. *Modern Physics Letters B* **2013**, *27*, 1330018.

(14) Woessner, A. et al. Near-field photocurrent nanoscopy on bare and encapsulated graphene. *Nat Commun* **2016**, *7*.

(15) Baugher, B. W. H.; Churchill, H. O. H.; Yang, Y.; Jarillo-Herrero, P. Optoelectronic devices based on electrically tunable p-n diodes in a monolayer dichalcogenide. *Nat Nano* **2014**, *9*, 262–267.

(16) Swanepoel, R. Determination of the thickness and optical constants of amorphous silicon. *Journal of Physics E: Scientific Instruments* **1983**, *16*, 1214.

(17) Terashima, K.; Imai, I. Indirect absorption edge of $ZrS_2$ and $HfS_2$. *Solid State Communications* **1987**, *63*, 315–318.

(18) Khodkov, T.; Khrapach, I.; Craciun, M. F.; Russo, S. Direct Observation of a Gate Tunable Band Gap in Electrical Transport in ABC-Trilayer Graphene. *Nano Letters* **2015**, *15*, 4429–4433.

(19) Roldan, R.; Castellanos-Gomez, A.; Cappelluti, E.; Guinea, F. Strain engineering in semiconducting two-dimensional crystals. *Journal of Physics: Condensed Matter* **2015**, *27*, 313201.

(20) Ferraro, J. R.; Nakamoto, K.; Brown, C. W. *Introductory Raman Spectroscopy*; Elsevier, 2003.

(21) Kolb, G.; Salbert, T.; Abstreiter, G. Raman-microprobe study of stress and crystal orientation in laser-crystallized silicon. *Journal of Applied Physics* **1991**, *69*, 3387–3389.

(22) Hart, T. R.; Aggarwal, R. L.; Lax, B. Temperature Dependence of Raman Scattering in Silicon. *Phys. Rev. B* **1970**, *1*, 638–642.

(23) Jellison, G. E.; Lowndes, D. H.; Wood, R. F. Importance of temperature-dependent optical properties for Raman-temperature measurements for silicon. *Phys. Rev. B* **1983**, *28*, 3272–3276.

(24) Urey, H. Spot size, depth-of-focus, and diffraction ring intensity formulas for truncated Gaussian beams. *Appl. Opt.* **2004**, *43*, 620–625.

(25) Self, S. A. Focusing of spherical Gaussian beams. *Appl. Opt.* **1983**, *22*, 658–661.

(26) Graham, M. W.; Shi, S.-F.; Ralph, D. C.; Park, J.; McEuen, P. L. Photocurrent measurements of supercollision cooling in graphene. *Nat Phys* **2013**, *9*, 103–108.

(27) Tielrooij, K. J.; Massicotte, M.; Piatkowski, L.; Woessner, A.; Ma, Q.; Jarillo-Herrero, P.; van Hulst, N. F.; Koppens, F. H. L. Hot-carrier photocurrent effects at graphene-metal interfaces. *Journal of Physics: Condensed Matter* **2015**, *27*, 164207.

(28) Mak, K. F.; Sfeir, M. Y.; Wu, Y.; Lui, C. H.; Misewich, J. A.; Heinz, T. F. Measurement of the Optical Conductivity of Graphene. *Phys. Rev. Lett.* **2008**, *101*, 196405.

(29) Bointon, T. H.; Jones, G. F.; De Sanctis, A.; Hill-Pearce, R.; Craciun, M. F.; Russo, S. Large-area functionalized CVD graphene for work function matched transparent electrodes. *Scientific Reports* **2015**, *5*, 16464, Article.

(30) Irkhin, P.; Ryasnyanskiy, A.; Koehler, M.; Biaggio, I. Absorption and photoluminescence spectroscopy of rubrene single crystals. *Phys. Rev. B* **2012**, *86*, 085143.

(31) Greenaway, D.; Nitsche, R. Preparation and optical properties of group IV-VI chalcogenides having the $CdI_2$ structure. *Journal of Physics and Chemistry of Solids* **1965**, *26*, 1445 – 1458.

(32) Malard, L.; Pimenta, M.; Dresselhaus, G.; Dresselhaus, M. Raman spectroscopy in graphene. *Physics Reports* **2009**, *473*, 51 – 87.

(33) Yoon, D.; Moon, H.; Son, Y.-W.; Samsonidze, G.; Park, B. H.; Kim, J. B.; Lee, Y.; Cheong, H. Strong Polarization Dependence of Double-Resonant Raman Intensities in Graphene. *Nano Letters* **2008**, *8*, 4270–4274.

(34) Chenet, D. A.; Aslan, O. B.; Huang, P. Y.; Fan, C.; van der Zande, A. M.; Heinz, T. F.; Hone, J. C. In-Plane Anisotropy in Mono- and Few-Layer $ReS_2$ Probed by Raman Spectroscopy and Scanning Transmission Electron Microscopy. *Nano Letters* **2015**, *15*, 5667–5672.

(35) Zeng, L.; Tao, L.; Tang, C.; Zhou, B.; Long, H.; Chai, Y.; Lau, S. P.; Tsang, Y. H. High-responsivity UV-Vis Photodetector Based on Transferable $WS_2$ Film Deposited by Magnetron Sputtering. *Scientific Reports* **2016**, *6*, 20343.

(36) Yao, J.; Zheng, Z.; Yang, G. Layered-material $WS_2$/topological insulator $Bi_2Te_3$ heterostructure photodetector with ultrahigh responsivity in the range from 370 to 1550 nm. *J. Mater. Chem. C* **2016**, –.

(37) Elías, A. L. et al. Controlled Synthesis and Transfer of Large-Area $WS_2$ Sheets: From Single Layer to Few Layers. *ACS Nano* **2013**, *7*, 5235–5242.

(38) Torres Alonso, E.; Karkera, G.; Jones, G. F.; Craciun, M. F.; Russo, S. Homogeneously Bright, Flexible, and Foldable Lighting Devices with Functionalized Graphene Electrodes. *ACS Applied Materials & Interfaces* **2016**, *8*, 16541–16545.

(39) Manzoor, K.; Vadera, S.; Kumar, N.; Kutty, T. Synthesis and photoluminescent properties of ZnS nanocrystals doped with copper and halogen. *Materials Chemistry and Physics* **2003**, *82*, 718 – 725.

(40) Alexander, F. ComponentLibrary. 2016; `http://www.gwoptics.org/ComponentLibrary/`, *Licensed under CreativeCommons Attribution-NonCommercial 3.0 Unported License*.